Neuroscience 596 (2026) 75–89

Contents lists available at ScienceDirect

Neuroscience

journal homepage: www.elsevier.com/locate/nsc

Modulatory effects of genetic vs. pharmacological HCN4 channel inhibition on stimuli transmission during acute pain

Maximilian Häfele [a,b], Natalia K. Freus [a], Silke Kreitz [a,c], Maria Novella Romanelli [d], Andreas Ludwig [a,b], Isabel Wank [a,*], Andreas Hess [a,b,c,*]

[a] Institute of Experimental and Clinical Pharmacology and Toxicology, Friedrich-Alexander-Universität Erlangen-Nürnberg, Fahrstraße 17, 91054 Erlangen, Germany
[b] FAU NeW – Research Center for New Bioactive Compounds, Friedrich-Alexander-Universität Erlangen-Nürnberg, Fahrstraße 17, 91054 Erlangen, Germany
[c] Institute of Neuroradiology, University Hospital Erlangen, Friedrich-Alexander-Universität Erlangen-Nürnberg, Schwabachanlage 6, 91054 Erlangen, Germany
[d] Department of Neurosciences, Psychology, Drug Research and Child Health, Section of Pharmaceutical and Nutraceutical Sciences, University of Florence, Viale Gaetano Pieraccini 6, 50139 Florence, Italy

ARTICLE INFO

Keywords:
HCN4 channels
Pain
BOLD-fMRI
Knockout mice
Pharmacological inhibition
EC18

ABSTRACT

Acute pain processing emerges from complex interactions among multiple brain regions, with local ion channels critically shaping neuronal communication. To better understand the role of HCN4 channels during acute pain in mice, a genetic brain-specific HCN4-KO was compared with pharmacological inhibition by the selective HCN4 channel blocker EC18.

Stimulus-driven BOLD-fMRI measurements using graded peripheral thermal stimulation allowed brain-wide investigation of both discriminative and suppressive processes within ascending and descending pain pathways. Classical BOLD parameters and graph-theoretical analyses revealed that compared to controls, HCN4-KO showed a significant increase in brain activity in regions responsible for discriminative tasks, emotional pain processing and pain suppression including sensory cortex, amygdala and hypothalamus across both high and low thermal stimulation intensities. In striking contrast, acute inhibition of HCN4 with EC18 decreased activity in these same regions compared with both KO and control mice.

Furthermore, comparing pre- and post-stimulation resting-state measurements revealed that HCN4-KO and controls exhibited a stimulation-induced increase in functional connectivity, whereas EC18-treated mice demonstrated a connectivity decrease.

Taken together, genetic loss of HCN4 produced a hypersensitive phenotype in thermal pain processing, whereas acute pharmacological inhibition of the channel elicited an opposing hyposensitive phenotype.

Introduction

Among the four isoforms of hyperpolarization-activated cyclic nucleotide-gated channels (HCN channels), HCN2 is well established as a key contributor to the development and maintenance of pathological pain, acting as a "pacemaker for pain" in nociceptive neurons (Emery et al. 2011; Schnorr et al. 2014; Herrmann et al. 2017; Tsantoulas, Mooney, and McNaughton 2016). HCN channels generate the I_h current, and the isoform most closely related to HCN2 is HCN4. The main difference between these two isoforms in biophysical terms is their activation kinetics: HCN2 activates considerably faster than HCN4 (Ludwig et al. 1999). Here, we explored if HCN4 channels also play a role in the

Abbreviations: HCN channels, Hyperpolarization-activated cyclic nucleotide-gated channels; HCN4-KO, HCN4 knockout; EC18, Pharmacological inhibition via EC18; Ctr, Control; BOLD, Blood oxygenation level dependent; fMRI, Functional magnetic resonance imaging; s-fMRI, BOLD fMRI with peripheral heat stimulation; RS-fMRI, Resting-state fMRI; EPI, Echo planar imaging; RARE, Rapid acquisition with relaxation enhancement; VOI, Volume of interest; RS_{pre}, Pre Resting-state; RS_{post}, Post Resting-state; SPMs, Statistical parametric maps; GLM, Generalized linear model; FDR, False discovery rate; ATPs, Average time profiles; IWV, Intensity weighted volume; TTP, Time to peak; AP, Activation probability; AUC, Area under the curve; NBS, Network-based statistics; FC, Functional connectivity; PAG, Peri aqueductal grey; VTA, Ventral tegmental area.

* Corresponding authors at: Institute of Experimental and Clinical Pharmacology and Toxicology, Friedrich-Alexander-Universität Erlangen-Nürnberg, Fahrstraße 17, 91054 Erlangen, Germany.

E-mail addresses: max.haefele@fau.de (M. Häfele), natalia.freus@fau.de (N.K. Freus), silke.kreitz@fau.de (S. Kreitz), novella.romanelli@unifi.it (M.N. Romanelli), andreas.ludwig@fau.de (A. Ludwig), isabel.wank@fau.de (I. Wank), andreas.hess@fau.de (A. Hess).

https://doi.org/10.1016/j.neuroscience.2026.01.011
Received 12 September 2025; Accepted 8 January 2026
Available online 9 January 2026

modulation of pain processing.

Nociceptive neurons express HCN1 and HCN2, but lack HCN4 (Schnorr et al. 2014). Whereas HCN2 is almost ubiquitously expressed in the brain, HCN4 displays a distinct spatial expression pattern. HCN4 channels are most abundant in thalamic and hypothalamic regions as well as in the olfactory bulb, but are also expressed in the basal ganglia, amygdala, hippocampus, prefrontal cortex, sensory input and the cerebellum (Moosmang et al. 1999; Santoro et al. 2000; Monteggia et al. 2000; Heintz 2004; Herrmann, Stieber, and Ludwig 2007; Hughes et al. 2013; Santos-Vera et al. 2019; Zuniga et al. 2016; Zobeiri et al., 2019). HCN4 channels control the excitability and rhythmicity of thalamocortical neurons and regulate thalamocortical oscillations (Zobeiri et al., 2019). Since sensory information entering the CNS is filtered and processed in thalamic regions before being relayed to upstream brain regions (Sherman and Guillery 2002), HCN4 channels are strong candidates for influencing the processing of stimuli like pain, presumably in an antinociceptive manner.

In a mouse model with a brain-specific HCN4 deletion, we previously observed altered processing of thermal nociceptive stimuli. Surprisingly, the HCN4 knockout resulted in a thermally hypersensitive phenotype (Häfele et al. 2023), contrary to expectations based on the presumed "pacemaker" function of HCN4 in the thalamus.

To further clarify the contribution of HCN4 to central pain processing, we compared the brain-specific HCN4-knockout to an acute pharmacological inhibition of HCN4. For this, we used the HCN4 blocker EC18 (Romanelli et al. 2019; Patberg et al. 2023), which has been shown to block HCN4 channels in a mouse model of epilepsy (Kharouf et al. 2020). We examined three groups – HCN4 knockout (HCN4-KO), acute pharmacological inhibition (EC18), and controls (Ctr) – using blood oxygenation level dependent (BOLD) functional magnetic resonance imaging (fMRI) combined with peripheral heat stimulation (s-fMRI), as well as resting-state fMRI (RS-fMRI) performed before and after the heat stimulation.

Based on classical brain region-specific BOLD response analyses, we identified brain regions involved in (noxious) heat processing across the different groups. Next, graph-theoretical analyses were performed on the heat stimulus-driven as well as on the resting-state measurements, providing a deeper insight into communication patterns and network dynamics across the whole brain and within individual regions.

Experimental procedures

Animal description and housing

Mouse lines were generated in our laboratory as described previously (Zobeiri et al., 2019). As the global HCN4 knockout is embryonically lethal (Stieber et al., 2003), we used floxed HCN4 mice (Stieber et al., 2003) crossed with the Nestin-Cre transgenic mice (Tronche et al. 1999) to achieve a brain-specific deletion of HCN4. Brain-specific HCN4 knockout mice carried the genotype $HCN4^{L2/L1}$, Nestin-$Cre^{tg/0}$, whereas littermate controls had the genotype $HCN4^{L2/+}$, Nestin-$Cre^{0/0}$. L2 indicates the floxed and L1 the floxed-out locus, respectively. All mice were maintained on a C57/BL6N background. Both male and female mice were used and housed separately in groups of up to five animals. The animals were kept in a 12-hour day/night cycle at 21 °C and food (Ssniff, Soest, Germany) and water were available *ad libitum*. To ensure full brain development, the experiments were carried out on animals that were at least 12 weeks old (Hammelrath et al. 2016). Data from both sexes were pooled for the analyses. For the MRI experiments, the group sizes were: Ctr: n = 12 (7 males; 5 females), HCN4-KO: n = 15 (7 males; 8 females) and EC18: n = 15 (5 males; 10 females).

The study complied with the ARRIVE guidelines and was conducted in accordance with Directive 2010/63/EU of the European Parliament and approved by the local regulatory authority (Regierung von Unterfranken) under license number RUF-55.2.2-2532-2-1460-16.

FMRI preparation

The animals were first anesthetized with 5 % isoflurane in medical air over a period lasting 2.5 to 3 min. The mice were then weighed in the anesthesia box. During the scans, anesthesia was maintained with 0.7–1.5 % isoflurane to ensure a respiration rate of 90–120 breaths per minute, guaranteeing optimal pCO_2 levels, BOLD contrast, and minimal head motion during the MRI measurement. To ensure a stable position of the mice during the measurement, the mice were mounted on an acrylic tray and were secured in a prone position. The tray was heated with warm water, to prevent hypothermia during the measurement under anesthesia. The front teeth of the mice were secured in a nose-mouth mask. This mask allowed a guaranteed supply of isoflurane for anesthesia during the measurement, and provided additional head fixation, minimizing the risk of head movement. To prevent exsiccation damage to the eyes during the measurement, an eye ointment was applied (Bepanthen, Bayer Vital GmbH, Leverkusen, Germany). Respiration was monitored with a pediatric respiration sensor (Graseby® Respiration Sensor, Smiths Medical, Inc., Minneapolis, MN, USA) which was placed under the abdomen of the mice. To deliver the thermal stimuli during the fMRI measurement, the right hind paw of the mice was placed and fixed with the dorsal side to a computer-controlled Peltier heating element. For signal detection and good signal-to-noise ratio, a 3 cm 4-channel array head coil (Bruker BioSpin MRI GmbH, Ettlingen, Germany) was placed directly above the brain of the mice.

Functional MRI

All s-fMRI and RS-fMRI scans were acquired on a 4.7 T Bruker BioSpec (Bruker BioSpin MRI GmbH, Ettlingen, Germany) with ParaVision (V. 7.0.0 Bruker BioSpin MRI GmbH, Ettlingen, Germany) as operating software. To verify a correct positioning of the mice within the scanner and to correct local field inhomogeneities, scout scans were obtained before the actual fMRI measurement. After those "positioning scans" a fast gradient-echo Echo Planar Imaging sequence (EPI; TR = 200 ms; TE_{eff} = 25 ms; FOV = 15 mm * 15 mm; 1 slice; slice thickness 0.5 mm; matrix 64 * 64 voxels) with 300 repetitions was performed. This sequence can be played back as a video to detect possible head motion, which may require positional corrections of the animals (movement > 1 voxel). These pre-adjustments were followed by an coronal rapid acquisition with relaxation enhancement (RARE) measurement (TR = 2000 ms; TE_{eff} = 56 ms; k-space averaging 4; RARE-Factor = 8; FOV = 15 mm * 15 mm; 12 slices; slice thickness 0.5 mm; matrix 128 * 128 voxels) serving as an anatomical template for positioning the volume of interest (VOI) of the following functional measurements (landmark: distal end of the lateral ventricle; VOI; 22 axial slices covering Bregma from −8.00 mm to 2.46 mm). To assess the image quality, this volume was acquired using EPI (TR = 2000 ms; TE_{ef} = 25 ms; FOV = 15 mm * 15 mm; slice thickness 0.5 mm; matrix 64 * 64 voxels; in-plane resolution of 0.234 mm * 0.234 mm). Resting-state scans were acquired before (RS_{pre}) and after (RS_{post}) thermal stimulation, each lasting 10 min with 300 volumes of these 22 slices. The s-fMRI measurement between both RS-measurements was acquired in a period of 50 min with 1500 volumes of the exact same 22 slices. A computer-controlled Peltier element (developed in-house) with active feedback and without interference from the MRI scanner allowed the stimulation temperatures to be achieved very accurately to within ± 1 °C. The baseline temperature of the Peltier device was 33.5 ± 1.3 °C. The thermal stimuli were applied to the right hind paw of the animals during s-fMRI. Each animal received three sets of four stimuli (40 °C, 45 °C, 50 °C, 54 °C). This variety of stimulation temperatures, where 40 °C and 45 °C are regarded as innocuous and 50 °C and 54 °C as noxious, enabled a detailed assessment of thermal perception and endogenous pain inhibition. The s-fMRI session began with 2 min of rest, after which each stimulus was presented for 20 s (5 s ramp, 15 s plateau) with an inter-stimulus interval of 3 min 40 s. After the RS_{post}-measurement, the mice were removed from the scanner.

The stimulated hind paw was treated with cooling foam spray (Bepanthen, Bayer Vital GmbH, Leverkusen, Germany) to prevent possible skin irritation caused by the thermal stimulation. The Animals were monitored in empty cages until fully awake before being returned to their home cages. The animals were euthanized following the last experiment by means of an overdose of CO2 and subsequent cervical dislocation.

Preparation and i.p. administration of EC18-solution in EC18 group

As EC18 reaches peak plasma levels 10 min after injection and is metabolized within 1 h (Kharouf et al. 2020), the substance was administered to C57/BL6N mice immediately before the RS_{pre} scan. The EC18 injection solution (10 mg/kg) was prepared according to (Kharouf et al. 2020). EC18 was delivered i.p. using a wing catheter (Venofix A® Venipuncture set, B. Braun Melsungen AG, Melsungen, Germany) inserted into the left side of the abdominal quadrant.

Data analysis

Stimulus-driven fMRI

Preprocessing and GLM-analysis

FMRI preprocessing was carried out using BrainVoyager QX (V. 2.0.8; Brain Innovation BV, Maastricht, Netherlands).

The first two volumes of each dataset were discarded to avoid saturation effects. Data preprocessing steps included slice scan time correction (ascending interleaved, interpolation method cubic spline), motion correction to eliminate brain movement (registration to first volume; trilinear detection and sinc interpolation), as well as spatial (Gaussian smoothing; kernel 2 pixels) and temporal smoothing (linear and non-linear high-pass filtering, kernel 12 s FWHM, FFT 9 cycles).

In order to obtain first-order statistical parametric maps (SPMs), a voxel-wise generalized linear model (GLM) analysis was employed to assess the coupling between stimulation and BOLD signal.

Each stimulation temperature was represented by its own predictor in the GLM analysis, which was folded with a mouse-specific two-gamma hemodynamic response function.

Further analysis was performed in MagnAn (BioCom GbR, Uttenreuth, Germany). For region level analysis, a self-developed mouse brain atlas was used. The atlas was created by selecting 22 slices from the Franklin and Paxinos' mouse atlas (Franklin and Paxinos 2008), that matched our grey-scale fMRI slices best. In total, 211 brain regions were identified, assigned to left and right hemispheres, and labeled with unique index numbers and color codes. Each atlas slice was aligned to the individual mouse anatomy using translational (x-y-z), scaling (x-y), and rotational (z) registration, producing subject-specific atlas masks for each animal, which served as basis for further analysis.

For each subject, the predictor-specific SPMs were binarized and corrected for multiple comparisons using false discovery rate (FDR; $q = 0.05$), and were then multiplied by the subject-specific atlas masks. For each brain region, average BOLD time profiles were calculated as the mean time courses of all voxels belonging to that region.

The stimulus-driven data were analyzed in two complementary approaches. For the more classical approach shortened average time profiles (ATPs) were generated for each brain region and predictor, consisting of 10 time points before, 10 during, and 10 after the stimulus. Subsequently, these ATPs were averaged over the three distinct stimulus representations.

Two key BOLD parameters were derived from the ATPs:

- Intensity weighted volume (IWV): the product of the activated brain volume [mm3] and the average signal change [%].
- Time to peak (TTP): the time required until the maximum signal amplitude was reached.

To focus the analysis, a subset of the 211 brain regions was pre-selected based on activation probability (AP). Only brain regions with an AP of at least 80 % for at least one of the four stimulus temperatures were included in the analysis.

This threshold was chosen because setting it at 90 % AP excluded several pain-relevant brain regions, whereas setting it below 80 % included too many regions, making meaningful presentation difficult.

Graph-theoretical analysis: creation of functional brain networks

In a graph-theoretical approach, brain networks were created (here for stimulation temperatures of 45 °C and 50 °C) in order to investigate their global network properties as well as their node-specific parameters. First, the global mean containing the stimulus responses (Fox et al. 2009) was removed using global signal regression. This was performed on the full-length time profiles of each predictor per subject. The Pearson correlation coefficient r was then calculated between the average time courses of all possible pairs of brain regions for each predictor and for each subject, resulting in symmetric adjacency matrices. The data were then transformed into normally distributed Fisher-z-values and average adjacency matrices were calculated per predictor and experimental group. After that, the Fisher-z-values were back-transformed into Pearson's r. The adjacency matrices represent brain networks and can be characterized using global properties and node-specific parameters (for detailed description see 2.6 – Explanation of graph-theoretical parameters – below).

To allow an accurate topological comparison of functional connectivity in a later step between the three groups (Ctr, HCN4-KO and EC18), all networks had to share the same density (i.e. the same number of connections). To determine the appropriate density, we first created networks with densities ranging from 2 % to 20 % in 2 % steps and recalculated the global parameters. The resulting 50 °C curve of the small world index sigma (global network efficiency), was then normalized to its maximum, and the vertex of the resulting hyperbola was calculated. At this vertex, here at a density of 6 %, the greatest changes within the network occurred. Consequently, all networks were restricted to the strongest 6 % of positive r-values **(Fig. S1A)**.

Resting-state fMRI

As with s-fMRI, the first two volumes were discarded. However, the pre-processing of the RS data was limited to slice scan time correction (ascending interleaved, interpolation method cubic spline) and motion correction (registration to first brain volume; trilinear detection and sinc interpolation).

Subsequent analysis steps were performed in MagnAn including a preprocessing step with bandpass filtering (high-pass filtering at 0.01 Hz and low-pass filtering at 0.1 Hz). The atlas masks were again created as described for the s-fMRI data. However, for RS, the atlas masks were cropped with individually drawn brain masks, to restrict the analysis to voxels within the brain.

The resting state connectivity was then analyzed using multi-seeded region analysis (MSRA), according to (Kreitz et al. 2018a), which includes the following steps: Starting with the positioning of a 0.5 mm^2 seed region in the center of gravity of the seed brain region, the Pearson correlation coefficient r between the average time course of the seed and all other voxels in the brain was determined. The result is one 3D correlation volume for each seed region, and the significant correlations were then identified by FDR ($q = 0.05$). To obtain an asymmetric connectivity matrix for each animal, the correlation volumes containing the r-values were first converted into Fisher z-values. Subsequently, the values of all voxels belonging to the same region were averaged for the respective seed. After repeating this step for each region of the atlas mask, the Fisher z-values were converted back to r-values at the end, yielding one row in the asymmetric connectivity matrix. These steps were repeated for each seed volume to create the full connectivity matrix.

Using the same procedure as for the s-fMRI data, the optimal network density was determined (here 7 %) and the networks were characterized

by analyzing both the network properties and the node parameters in the same way as for the s-fMRI.

Explanation of graph-theoretical parameters

Global network parameter – (characterization of interactivity and efficacy of the whole brain network)

To obtain a global overview of the network properties within each experimental groups, the area under the curve (AUC) was calculated for each network parameter **(Fig. S1B).** These AUC values were then used to generate a characteristic "fingerprint" of the global network properties for each group **(**Fig. 3**)**. To enhance interpretability, the parameters were organized into four categories:

1. Quantitative parameters

This category includes the **number of nodes**, and the network **strength** – the sum of all connection weights (Fishers z) associated with a node. The strength can be subdivided into the **mean nodestrength** (mean strength of the nodes) and the **mean edge strength** (mean strength of all connections).

2. resiliency/robustness

Describes the susceptibility or resistance of a network to random errors or targeted attacks.

Degree assortativity and **vertex similarity** quantify whether individual nodes tend to connect preferentially to nodes with similar properties (Newman 2002; Leicht, Holme, and Newman 2006). Higher values reflect increased robustness to node removal. **Natural connectivity** and **natural radius** describe the availability and number of alternative path loops within the network (Jun et al. 2010; Freitas et al. 2022). More alternative path loops indicate a structurally more resilient network. The parameter **natural gap** reflects the tendency of a network to form bottlenecks (Estrada 2006). A high natural gap value indicates fewer potential bottleneck structures and therefore greater robustness.

3. segregation/integration

These **metrics** quantify how information is distributed within the network. In this regard, the **clustering coefficient** represents the average proportion of existing connections among each node's direct neighbors. The **average shortest path** measures the minimal number of steps required to travel along a connection path between any two nodes in the network. Isolated nodes are ignored for both parameters. The **performance** is defined as the sum of all connection paths divided by the total number of all possible connections (Wang, Zhang, and Yue 2018). Isolated and unreachable nodes are also included and contribute a value of 0.

4. Effectivity/small worldness

The small world index **sigma** – quotient between **gamma** and **lambda** – serves as a measure for the efficiency of information transfer within a network (Watts and Strogatz 1998).

Gamma is defined as the clustering coefficient normalized to the mean clustering coefficient of a defined number of random networks and **lambda** as the average shortest path normalized to the mean average shortest path of those random networks.

Node-specific parameter – characterization of interaction and efficacy of single brain regions

Beyond global network differences, region-specific characteristics were investigated by analyzing the node-specific parameters. As for the analysis of the BOLD parameters, a preselection step was applied to focus on the most important brain regions. Only those brain regions in which at least 10 % of all animals showed a degree value greater than 0 and had an average degree of at least 10 were included. The differences were analyzed using a two factor ANOVA for each node-specific parameter. Possible interactions between the phenotype and brain region factors for the individual node parameters were examined. Follow-up onefactor ANOVAs were therefor conducted to identify specific brain regions showing significant differences for the node parameters.

The investigation of the node-specific parameters focused on the parameters average node strength, node degree, clustering coefficient, pathlength, betweenness, hubscore, VIP index, hub participation, vertexload and vulnerability. However, only parameters with a significant main effect and significant phenotype and brain region interaction are reported in detail.

The **node strength** shows the sum of the correlation values of all connections per node. The **clustering coefficient** and **shortest path** parameters are both important for assessing the integration and segregation of networks. The clustering coefficient is defined as the relative number of connections between the direct neighbors of a node, while the average shortest path indicates the average of the minimum number of steps required to reach all other nodes within the network. A low shortest path length and a high clustering coefficient together indicate efficient local integration and rapid information distribution, while a higher shortest path combined with low clustering coefficient values describe a wider distributed and more segregated network.

The importance of a node in a network can be described by the parameters hubscore and VIP index. The **hubscore** is a measure for the hub-functionality of a node, i.e. the importance of a node for efficient information distribution. Hubs can be further characterized by the **VIP index**, distinguishing isolated nodes (low values) from highly connected hub-like nodes whose neighbors also have many connections.

The parameters vertexload and vulnerability provide insight into the overall robustness of the network. **Vertexload** – calculated as the product of a node's degree and the sum of its neighbors' connections – reflects how changes in the distribution of individual vertex loads may indicate changes in network robustness. **Vulnerability** describes how much the network's performance declines when a particular node is removed (Wang, Zhang, and Yue 2018). A high vulnerability value indicates that removing the node greatly impairs the network, highlighting the node's importance for overall network integrity.

Statistic

Classical BOLD parameters and node-specific parameters were tested for group differences (HCN4-KO, Ctr, EC18) using a two factor ANOVA. A Tukey ($p < 0.05$) was used as a post hoc test. A one factor ANOVA was performed as a follow-up when interactions were found.

Differences between the mean networks of the experimental groups can be analyzed using Network-based statistics (NBS) (Zalesky, Fornito, and Bullmore 2010). Depending on the group comparison, either a homoscedastic or paired Student's T-test ($\alpha = 0.05$) was first performed based on the individual animal matrices. The result is a difference matrix or a network containing all statistically significant connections.

In this network, the largest contiguous node cluster was then identified based on its number of connections. The individual animal matrices of the compared groups were then randomly reassigned to two groups and the *t*-test was recalculated. This randomization process was repeated 1000 times. The number of tests in which the largest node cluster exceeded that of the original *t*-test was noted, and in the next step divided by the number of test repetitions (1000) to determine the corrected p-value. Differences in the original *t*-test were only considered statistically significant if the thereby determined p-value was less than 0.05.

Visualization

The adjacency matrices were visualized as networks using the software Amira (V. 5.4.2 Thermo Fisher Scientific Inc., Waltham, USA) combined with custom programmed visualization modules. The individual brain regions are shown as color-coded nodes positioned approximately according to their anatomical position within a transparent 3D brain.

Correlation coefficients are represented as edges connecting the

nodes. The node size reflects the number of individual connections each node has (i.e. its degree value). Isolated nodes without any connection were omitted from the visualization. The blue and red edge colors indicate outcomes of the statistical tests performed with NBS. The specific meaning of the color coding is explained in the corresponding figure legends.

Randomization and blinding

In general, the order of the animals from the different experimental groups, measured on the same day was randomized to avoid potential daytime effects. The experimenter was aware of the phenotype of the test animals at all times, but animals from all three groups were analyzed together in batches in standardized workflows that neither required nor permitted experimenter input, ensuring unbiased handling.

Results

Study design

Three separate fMRI measurements were conducted within a single session (Fig. 1). First, a RS_{pre} measurement was performed, followed by the heat-stimulus-driven fMRI, and finally a RS_{post} measurement to assess the stimulation's impact on brain processing. The heat stimulus comprised three sets of progressively increasing heat stimuli: 40 °C and 45 °C (innocuous temperatures) and 50 °C and 54 °C (noxious heat).

s-fMRI analysis

To gain an initial overview of how HCN4 channels influence acute nociceptive processing, the s-fMRI data of the three animal groups was characterized by classical BOLD response parameters, which remained stable throughtout the entire 50 min time course (Fig. S2). This analysis included whole-brain IWV (a measure of overall activation strength), followed by the two parameters TTP and general AP.

BOLD responses to heat stimulation were significantly enhanced by the HCN4 knockout, but reduced after treatment with EC18

A two factor ANOVA conducted for each stimulation temperature revealed significant main effects among all three groups at 40 °C, 45 °C and 50 °C, but not at 54 °C. Significant differences for IWV were most prominent at 45 °C and 50 °C (Fig. 2A). While HCN4-KO showed significantly higher IWV values for the stimulation temperatures 40 °C and 45 °C compared to the two other groups, the difference between

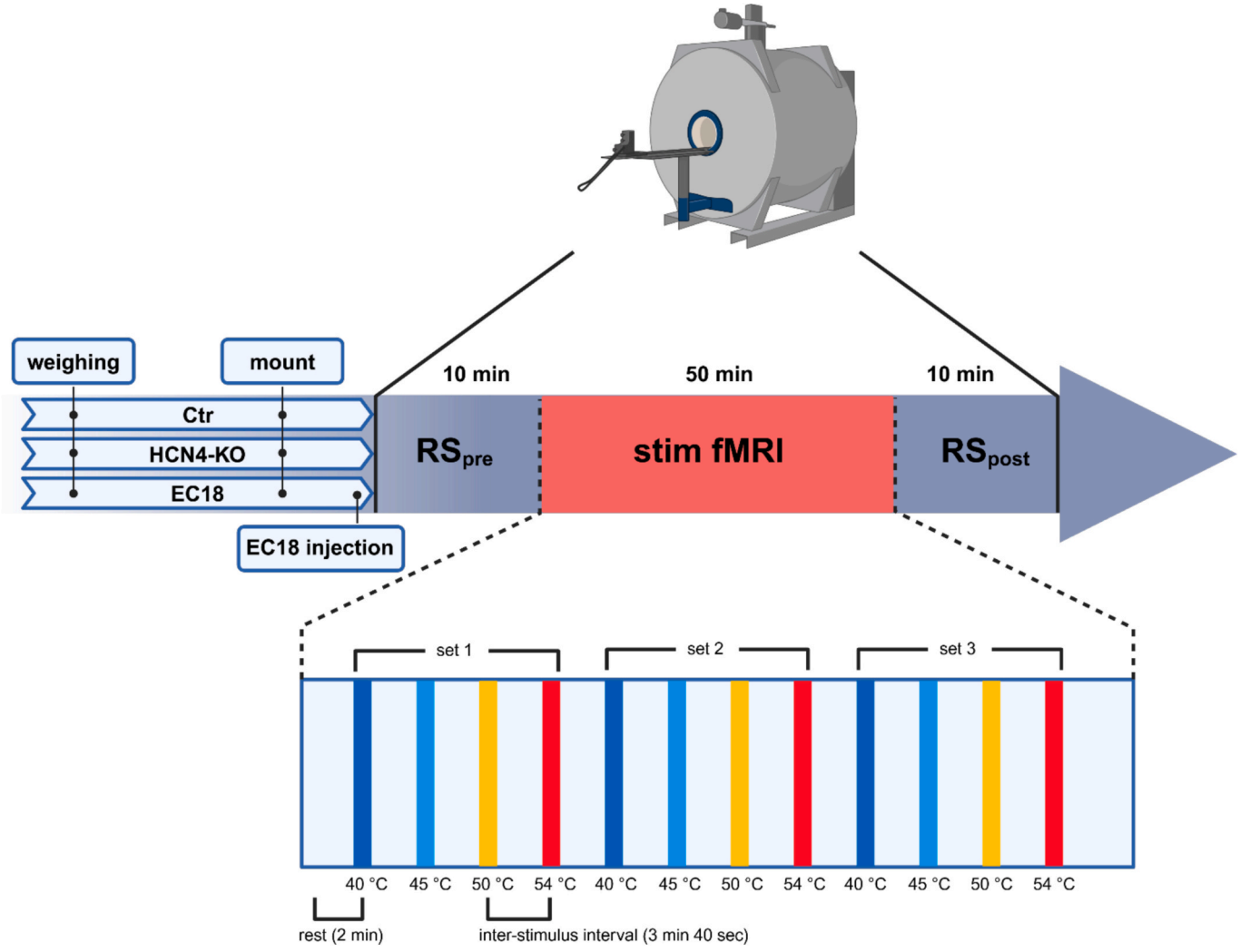

Fig. 1. Study design. The animals were weighed and mounted on an acrylic tray for the MRI measurement. The mice in the EC18 group were injected with the EC18 injection solution directly before the start of the initial 10-minute resting-state measurement (RS_{pre}). The RS_{pre} measurement was followed by the 50-minute functional MRI measurement with heat stimulation (s-fMRI). During heat stimulation, 3 sets of staggered increasing heat stimuli (40 °C, 45 °C innocuous; 50 °C and 54 °C noxius) were applied to the animals' right hind paw. The s-fMRI measurement was again followed by a 10-minute resting-state measurement (RS_{post}). Created in BioRender. Wank, I. (2025) https://BioRender.com/t44b106.

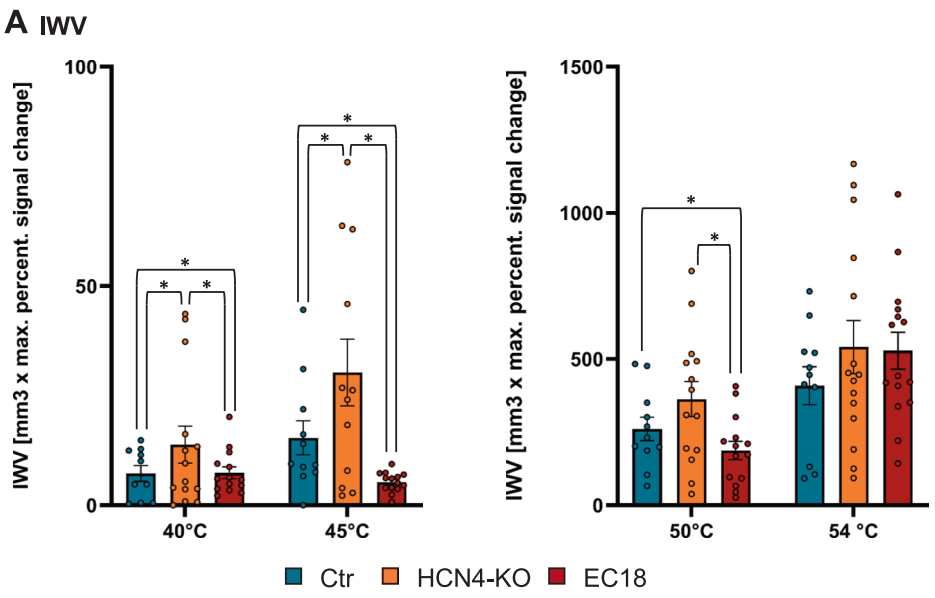

B Significant interactions for IWV 45 °C and 50 °C

45 °C

functional group	brain region	Ctr	HCN4-KO	EC18	sig.
brainstem	PCRt-r	0.46	9.85	0.10	0.03
sensory input	TN-r	0.92	11.00	0.37	0.02
sensory input	TN-l	0.64	14.80	0.10	0.03
sensory input	VTA-r	0.74	3.23	0.11	0.04
sensory input	VTA-l	0.21	3.14	0.24	0.01
sensory input	CF-r	0.37	2.69	0.11	0.03
sensory input	IC-r	7.25	66.46	3.58	0.02
sensory input	IC-l	3.42	46.60	2.71	0.03
sensory input	IP	0.68	3.37	0.48	0.03
sensory cortex	cxS1HL-l	2.53	11.05	0.59	0.02
sensory cortex	cxS1FL-l	2.16	6.74	0.55	0.01
sensory cortex	cxS1DZ-l	0.82	3.18	0.25	0.01
sensory cortex	cxS1ULp-l	1.11	8.35	1.93	0.00
sensory cortex	cxS1BF-l	4.99	36.76	3.59	0.01
sensory cortex	cxS1Sh-l	0.39	3.94	0.07	0.04
sensory cortex	cxS1Tr-l	0.88	12.72	0.26	0.02
sensory cortex	cxS1r-l	1.24	4.46	0.37	0.02
sensory cortex	cxS2-r	7.30	12.86	1.42	0.02
sensory cortex	cxAu-l	1.50	28.15	4.33	0.02
motor cortex	M1-l	3.29	9.01	0.64	0.04
association cortex	cxCg-r	7.25	2.41	0.82	0.05
association cortex	cxCg-l	6.03	2.24	0.59	0.03
limbic system unspecific	DB-l	0.92	7.91	0.16	0.03
hippocampus	hcSV-r	5.19	7.55	0.57	0.05
amygdala	amCe-l	0.41	5.06	0.16	0.02
hypothalamus	hyPV	1.13	4.20	0.04	0.03
basalganglia	GPL-l	0.46	4.10	0.91	0.03
cerebellum	CbVe-r	6.30	121.50	4.46	0.00
cerebellum	CbVe-l	9.32	102.32	2.50	0.04
cerebellum	CbPVe-r	8.89	69.12	4.18	0.01
cerebellum	CbFPF-r	6.68	16.95	0.58	0.06
cerebellum	CbDN-r	2.12	11.38	0.06	0.04

50 °C

functional group	brain region	Ctr	HCN4-KO	EC18	sig.
olfactory niput	ON-l	54.11	114.81	22.46	0.02
olfactory niput	OT-l	58.24	135.47	35.21	0.02
sensory cortex	cxS1DZ-l	18.65	11.43	4.47	0.06
sensory cortex	cxS1Sh-l	15.66	12.45	4.12	0.05
motor cortex	M2-r	53.87	25.02	14.27	0.04
motor cortex	M2-l	91.74	42.40	19.29	0.02
association cortex	cxTeA-l	97.68	115.18	37.50	0.02
association cortex	cxPrL-l	12.00	34.31	7.75	0.03
association cortex	cxPdD-r	7.89	16.91	6.24	0.03
association cortex	cxPdD-l	6.60	18.44	4.82	0.01
association cortex	cxOrb-r	37.62	143.76	23.62	0.03
association cortex	cxOrb-l	48.45	161.33	30.83	0.02
association cortex	cxFrA-l	20.38	43.98	5.65	0.01
link to the limbic	cxPir-r	421.41	616.84	165.57	0.05
link to the limbic	cxPir-l	279.37	450.07	132.94	0.05
limbic system unspecific	Hb-r	15.50	5.15	5.28	0.02
amygdala	amBM-r	39.70	69.40	13.24	0.01
amygdala	amBM-l	24.37	38.33	9.89	0.06
amygdala	amBL-r	72.87	92.91	20.28	0.04
amygdala	amCe-l	10.30	23.94	2.43	0.02
hypothalamus	hyPV	4.19	17.51	7.29	0.01

Fig. 2. Analysis of the BOLD response parameter IWV, (a) Intensity weighted brain volume (IWV) in mm^3 x max. percent. Signal change ± SEM; (*$p < 0.05$ was determined by two factor ANOVA with a Tukey as post hoc test; 40 °C (F (2, 7449) 17.186, $p < 0.001$, $\eta 2_p = 0.0045$), 45 °C (F (2, 7449) 129.794, $p < 0.001$, $\eta 2_p = 0.0336$), 50 °C (F (2, 7449) 88.475, $p < 0.001$, $\eta 2_p = 0.0232$), 54 °C (F (2, 7449) 0.828, $p < 0.437$, $\eta 2_p = 0.0002$)), (Ctr., n = 12; HCN4-KO, n = 15 and EC18, n = 15)). Significant differences were found for IWV at 40 °C, 45 °C and 50 °C stimulus temperatures. HCN4-KO showed significantly increased IWV compared to EC18 and Ctr especially at low temperatures (40 °C and 45 °C). EC18 on the other side showed significantly reduced IWV at 40 °C, 45 °C and 50 °C. (b) Significant interaction between HCN4-KO, Ctr and EC18 for IWV at stimulation temperature at 45 °C and 50 °C. The two factor ANOVA revealed significant interactions for IWV at 45 °C ((F (380, 7449) 1.898, $p < 0.001$, $\eta 2_p = 0.0882$) and 50 °C (F (380, 7449) 1.229, $p < 0.001$, $\eta 2_p = 0.0621$). Specific brain regions were identified using a one factor ANOVA ($p < 0.05$) as follow-up. HCN4-KO showed significantly higher IWV in general but particularly in regions of sensory input, sensory cortex and cerebellum at 45 °C and in association cortex and amygdala at 50 °C. EC18 on the other hand showed significantly decreased IWV in the aforementioned regions and in general compared to Ctr but especially in contrast to HCN4-KO.

HCN4-KO and Ctr was no longer significant at 50 °C. In contrast, the EC18 group displayed significantly lower values than both HCN4-KO and Ctr at these stimulation temperatures.

In addition, the two factor ANOVA also revealed interactions for IVW between the factors phenotype and brain region for IWV at 45 °C and 50 °C. To identify individual brain regions, a follow-up one factor ANOVA was performed (Fig. 2B). At 45 °C (brainstem, sensory input, cortex and cerebellum) and at 50 °C (olfactory input, cortex, amygdala), HCN4-KO showed the highest values in most cases. Conversely, EC18 exhibited significantly lower values in nearly all regions compared to Ctr, and even more so compared to HCN4-KO (Fig. 2B).

HCN4-KO accelerated BOLD response, while EC18 treatment delayed it

Significant differences in TTP were observed at stimulation temperatures of 40 °C, 50 °C and 54 °C (Fig. S3A). At 40 °C and 54 °C, HCN4-KO exhibited the shortest TTP. For 50 °C and 54 °C, EC18-treated animals showed significantly longer TTP values compared to HCN4-KO and Ctr.

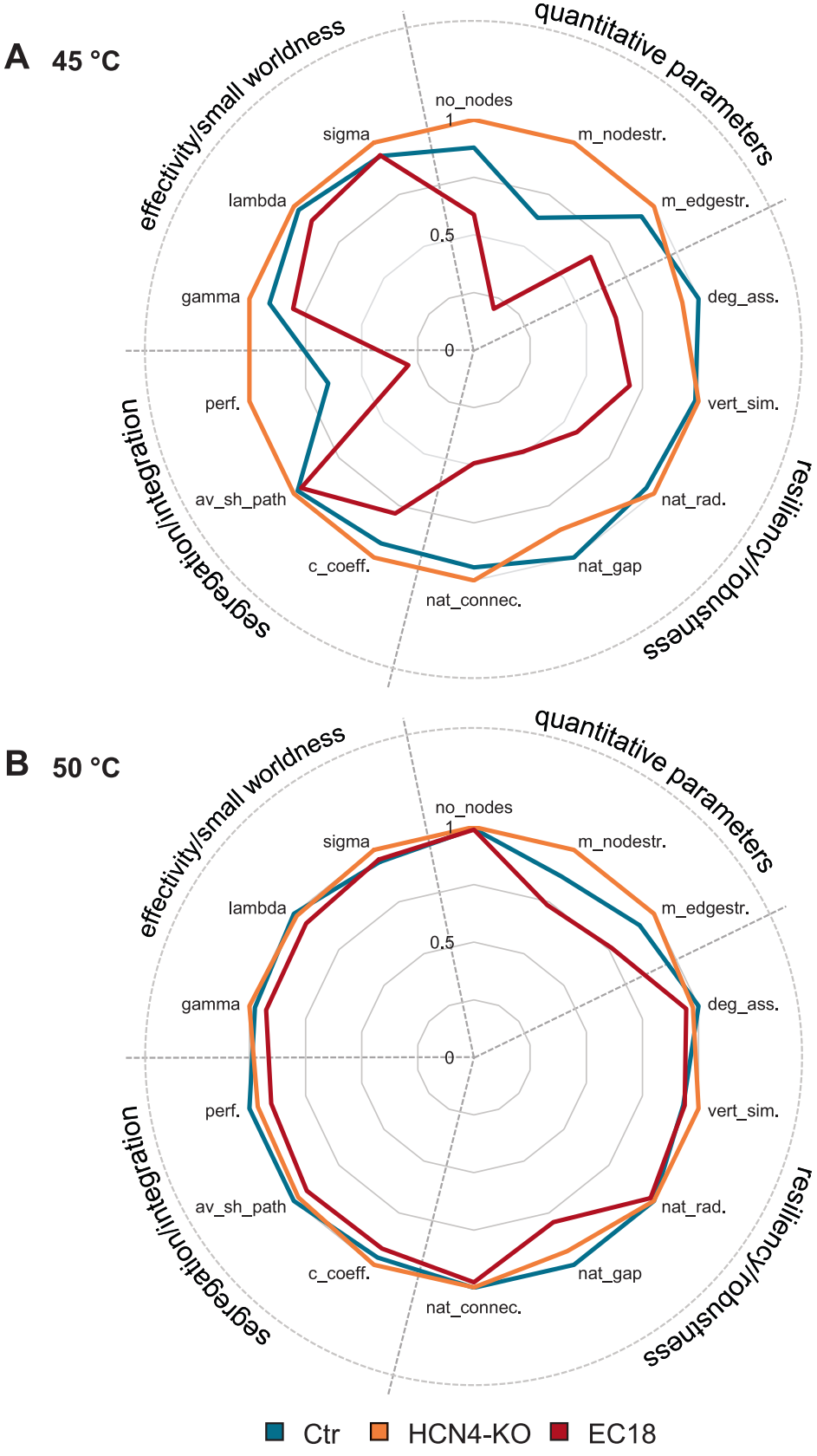

(caption on next page)

Fig. 3. Fingerprint of the network parameters for stimulus driven fMRI. The fingerprint results from the averaged AUC of the network parameters of the individual groups (normalized to the maximum value of the individual parameters per temperature). Clear differences in the fingerprints of the network parameters between the groups indicate a different modulation of information processing. (a) 45 °C: Fingerprints of Ctr and EC18 showed similar feature characteristics, with a pronounced reduction in EC18. There were clear differences to the fingerprint of HCN4-KO in particular. (b) 50 °C: Fingerprints of Ctr and EC18 were almost identical – there were still major differences to the fingerprint of HCN4-KO. Abbreviations: number of nodes **(no_nodes),** mean node strength **(m_nodestr.),** mean edge strength **(m_edgestr.),** degree assortativity **(deg_ass.),** vertex similarity **(vert_sim.),** natural radius **(nat_rad.),** natural gap **(nat_gap),** natural connectivity **(nat_connec.),** clustering coefficient **(c_coeff.),** average shortest path **(av_sh_path),** performance **(perf.)**.

Neither HCN4-KO nor treatment with HCN4 blocker EC18 influenced general brain excitability

No significant differences in AP were found among the three groups (**Fig. S3B**). Because classical BOLD analysis does not allow direct conclusions about interaction of brain regions over time, we complemented it with graph-theoretical analyses to obtain a more dynamic perspective of the information flow across the entire brain. This approach provided a detailed insight into the communication between individual brain regions, enabling a deeper assessment of the role of HCN4 in functional connectivity.

Graph-theoretical analyses revealed an impact on brain network efficacy for HCN4-KO and EC18

We focused the graph-theoretical analysis on the temperatures 45 °C and 50 °C, as the threshold between warmth and heat sensation lies within this range (Wank et al. 2022). Moreover, at 54 °C and above endogenous descending pain inhibition is expected to be active (You et al. 2014).

In (Fig. 3), the fingerprints for the AUC values of various graph-theoretical measures (for detailed description see Methods 2.6 – Explanation of graph-theoretical parameters) are depicted. Those fingerprints were highly similar for HCN4-KO at 54 °C and 50 °C. Moreover, Ctr and EC18 shared the same pattern of feature distribution at 45 °C, but EC18 showed markedly lower AUC values. The most pronounced difference in feature distribution between HCN4-KO and Ctr/EC18 comprised quantitative parameters and the segregation/integration category **(**Fig. 3A**)**.

At 50 °C, the fingerprints of all three groups were largely comparable, with differences primarily in quantitative parameters and resiliency/robustness category. At 50 °C, EC18 showed slightly lower AUC overall compared to Ctr and HCN4-KO, particularly in these two categories **(**Fig. 3B**)**.

Genetic and pharmacological loss of HCN4 differentially modulated network properties of specific brain regions

Beyond the global differences, an analysis of the node-specific parameters using a two factor ANOVA for each node-specific parameter revealed significant main effects between the groups, at both stimulation temperatures (45 °C and 50 °C) **(**Table S1**)**.

For parameters showing a main effect, the two factor ANOVA also identified significant interactions, at 45 °C for the parameters **strength**, **vertex load** and **pathlength (**Table S2**A)**, and at 50 °C for **clustering coefficient**, **pathlength**, **hubscore** and **VIP index (**Table S2**B)**. The specific brain regions contributing to these effects were identified using a one factor ANOVA as follow-up**.** Respective percentage differences for the individual brain regions are summarized in **(**Table S3**).**

45 °C:

At 45 °C, a clear pattern emerged: HCN4-KO displayed the highest values across nearly all graph-theoretical parameters in the vast majority of brain regions, while EC18 consistently showed the lowest values **(**Table S2**A)**.

For **strength**, differences were found in the limbic system, amygdala, hypothalamus, basal ganglia, and especially in the cerebellum. The differences in **vertex load** appeared in the brain stem, sensory input, hippocampus, amygdala, basal ganglia, and cerebellum. In **pathlength**, differences were particularly concentrated in regions of brainstem and amygdala, but also emerged in sensory input, hypothalamus, limbic output, and cerebellum.

50 °C:

At 50 °C the pattern was less uniform. Ctr – and occasionally EC18 – showed higher values than HCN4-KO, especially for the **clustering coefficient** and **hubscore** parameters **(**Table S2**B)**.

For the **clustering coefficient**, the significant differences occurred in olfactory input, thalamus, associative cortex, amygdala, hypothalamus, and basal ganglia. Differences in **pathlength** were identified in the olfactory input, associative cortex, limbic cortex, hippocampus, hypothalamus, and the cerebellum. The **hubscore** parameter showed differences in sensory input, sensory cortex, limbic cortex, amygdala, basal ganglia, and cerebellum. For the **VIP index**, the focus of differences was concentrated primarily on the amygdala, where HCN4-KO showed the highest values. However, differences between groups were also observed in the limbic cortex, the limbic output, and the cerebellum.

Pharmacological HCN4 blockade with EC18, but not genetic KO of HCN4, modulated interactions between brain regions

Network-based statistics can be used to assess the flow of information and information processing in and between brain regions based on differences in their functional connectivity (FC). These differences can be visualized as 3D networks **(**Fig. 4**).** For topological comparability, all networks were thresholded to a uniform density of 6 %, based on the analysis of the small world characteristics (see Methods 2.5.1 – Stimulus-driven fMRI) **(**Fig. S1**A)**. Significant differences were detected for HCN4-KO vs. EC18 at both 45 °C and 50 °C, and for EC18 vs. Ctr at 45 °C. In contrast, differences between HCN4-KO and Ctr did not reach the significance at either temperature.

At 45 °C, significant differences between EC18 and Ctr, were primarily located in areas of sensory input, hippocampus, hypothalamus, sensory, and motor cortex. When comparing HCN4-KO and EC18 at 45 °C, areas of the sensory input, thalamus, sensory and associative cortex, hippocampus, hypothalamus, and cerebellum stood out in particular. Across nearly all regions – with the exception of a few sensory cortical areas – HCN4-KO showed significantly higher FC compared to EC18 at 45 °C and 50 °C, especially in areas of sensory input, thalamus, amygdala, hypothalamus and hippocampus.

Stable but reduced BOLD signal in EC18 across s-fMRI measurement

An analysis of the BOLD signal amplitude in the somatosensory cortex during the s-fMRI measurement revealed stable responses across all three groups. Compared to Ctr and especially HCN4-KO, EC18 showed a consistently weaker BOLD signal throughout the 50 min acquisition (Fig. S2).

RS-fMRI analysis

To assess information processing at rest, resting-state fMRI measurements were performed before and after the s-fMRI measurement. The RS data were analyzed using two complementary approaches.

First, global network- and node-specific properties were compared between the three individual groups separately for RS_{pre} and RS_{post} measurements. Second, the potential influence of the intermediate stimulation on resting-state brain activity was examined by comparing RS_{pre} to RS_{post} within each group. As for the s-fMRI measurement the network density for RS-measurement was determined (7 % for RS-measurement), and all networks were thresholded to this density for visualization.

Pharmacological inhibition by EC18 affected general brain functions in post resting-state, while genetic HCN4-KO did not

The fingerprints characterizing the global network properties for the

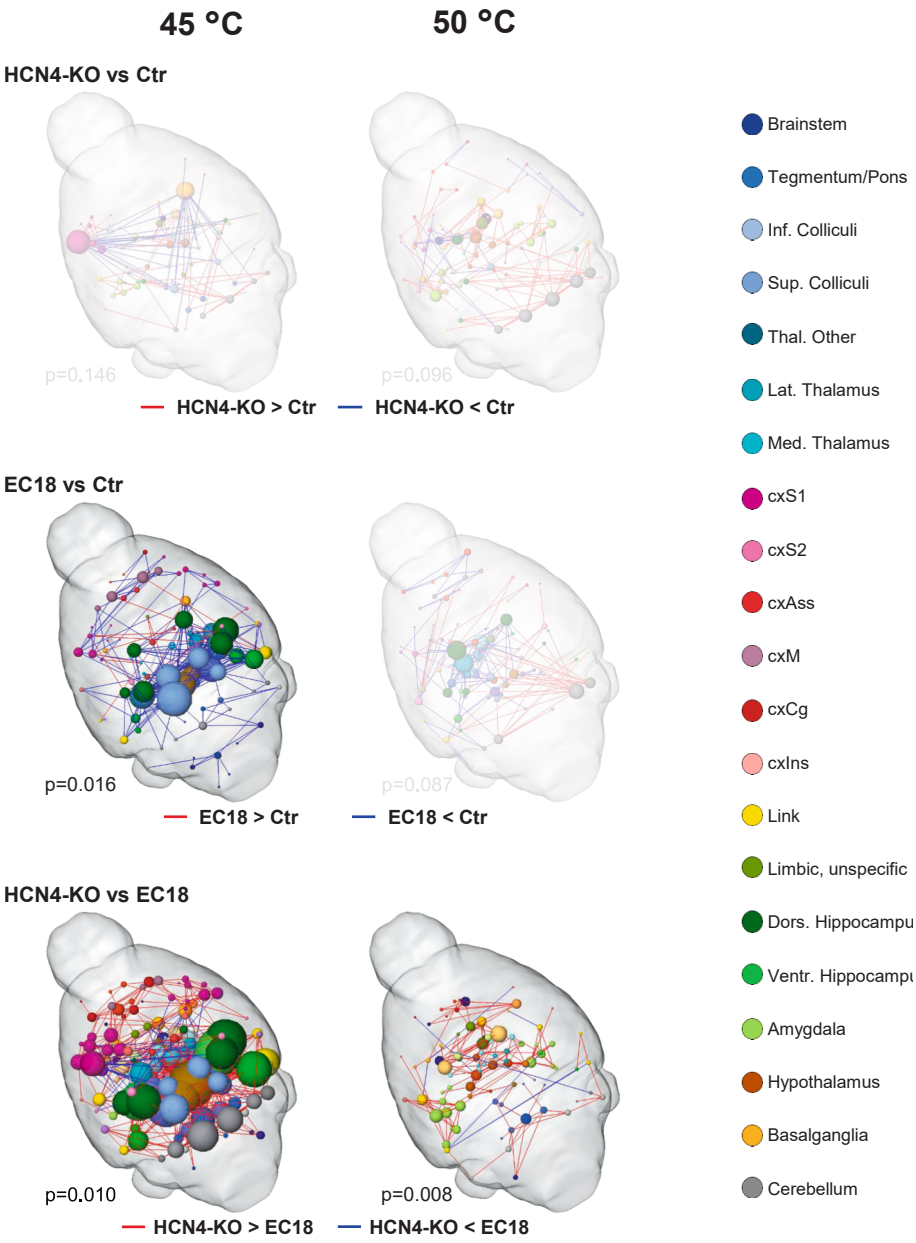

Fig. 4. Differences in functional connectivity for s-fMRI measurement The differences were calculated using network-based statistics, (p-values as indicated) and displayed as 3D-networks within a transparent brain surface. The 211 brain regions are visualized by the color-coded nodes (orphaned nodes are not shown). The edges between the individual nodes represent the detected differences in functional connectivity (meaning of the color-coded nodes and edges can be seen in the figure). No significant differences in FC between HCN4-KO and Ctr. EC18 showed at significantly lower FC 45 °C compared to Ctr and HCN4-KO especially in regions of sensory input (inferior and superior colliculi), sensory cortex, hippocampus and hypothalamus. At 50 °C, EC18 showed significantly lower FC only compared to HCN4-KO in amygdala and hypothalamus. Abbreviations: primary somatosensory cortex **(cxS1)**, secondary somatosensory cortex **(cxS2)**, association cortex **(cxAss)**, motor cortex **(cxM)**, cingulate cortex **(cxCg)**, insular cortex **(cxIns)**.

RS_{pre} and RS_{post} revealed several key findings **(**Fig. 5**)**. First, in RS_{pre}, the fingerprints of Ctr and EC18 closely match each other except in resiliency/robustness category, where EC18 showed higher values. Second, both Ctr and EC18 showed subtle but consistent differences from HCN4-KO across all four parameter categories. Third, from RS_{pre} to RS_{post}, the fingerprints of Ctr – and particularly EC18 – changed markedly, whereas the fingerprints of HCN4-KO remained highly stable. And fourth, in RS_{post}, the fingerprints of HCN4-KO and Ctr were nearly identical, while EC18 showed pronounced deviations, with substantially lower AUC values for almost all parameters except those in the segregation/integration category.

Analysis of the node-specific parameters revealed significant interactions for hubscore

As with the s-fMRI measurement, the node-specific parameters were also examined for the RS-measurements in addition to the global network parameters. In both RS_{pre} and RS_{post}, a two factor ANOVA for each node-specific parameter revealed significant main effects for all three phenotypes **(**Table S4**)**.

Furthermore, significant interactions were identified by the two factor ANOVA for the parameter hubscore in both RS_{pre} and RS_{post}. Here too, a one factor ANOVA was used as follow-up to determine significantly differing brain regions **(**Table S5**)**. The percentage differences for individual brain regions are listed in **(**Table S6**)**.

RS_{pre}:

Significant differences were found in the RS_{pre} **(**Table S5**A)** particularly in regions of the brainstem, sensory and associative cortex, limbic

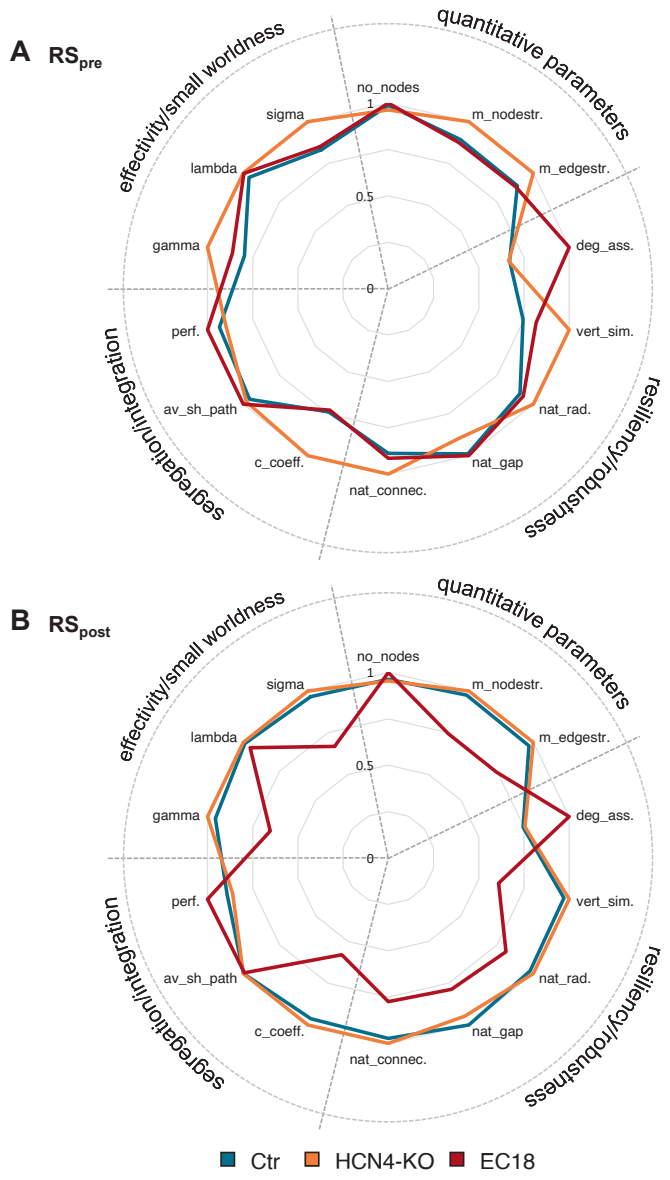

Fig. 5. Fingerprint of the network parameters for resting-state fMRI The fingerprint results from the averaged AUC of the network parameters of the individual groups, which were normalized to the maximum value of the individual parameters for RS_{pre} on the one hand and RS_{post} on the other. Clear differences in the fingerprints of the network parameters between the groups indicate a different modulation of information processing. (a) RS_{pre}: In particular, the fingerprint of HCN4-KO differed noticeably from that of Ctr and EC18. The fingerprint of Ctr is similar to that of EC18, but somewhat less pronounced. (b) RS_{post}: In the RS_{post}, the fingerprints of HCN4-KO and Ctr were almost identical. The fingerprint of EC18, however, clearly differed from those of the other two groups. Abbreviations: number of nodes **(no_nodes),** mean node strength **(m_nodestr.),** mean edge strength **(m_edgestr.),** degree assortativity **(deg_ass.),** vertex similarity **(vert_sim.),** natural radius **(nat_rad.),** natural gap **(nat_gap),** natural connectivity **(nat_connec.),** clustering coefficient **(c_coeff.),** average shortest path **(av_sh_path),** performance **(perf.)**.

system, and cerebellum. EC18 showed the highest values in both the brainstem and the cerebellum. In cortical areas on the other hand, Ctr displayed the highest values, while HCN4-KO exhibited the strongest values in limbic regions.

RS_{post}:

In RS_{post} **(Table S5B),** significant differences were concentrated in cortical regions, especially the associative cortex. HCN4-KO and Ctr predominantly showed the highest values in associative cortex, whereas EC18 exhibited the highest values in brainstem and sensory cortex. Additionally, Ctr was dominant in the hippocampus, while HCN4-KO had the highest values in the basal ganglia.

FC analysis for RS_{post} showed reduced impact of 'heat pain processing' by EC18 compared to HCN4-KO and Ctr

To evaluate if and how heat stimulation modulates resting-state for HCN4-KO and EC18 compared to Ctr, differences in FC for RS_{post} vs RS_{pre} were analyzed by NBS and visualized as 3D networks (Fig. 6).

Comparisons with Ctr did not yield significant differences for HCN4-KO in either RS_{pre} or RS_{post}, nor for EC18 in RS_{pre}. In contrast, the RS_{post} comparison Ctrl vs EC18 showed significant differences. With the exception of several associative cortical regions, EC18 exhibited generally a significantly lower FC relative to Ctr, especially within the peri aqueductal grey (PAG), regions of sensory input, sensory cortex and hippocampus (Fig. 6**, middle right column, dominant blue edges)**.

Next, comparing HCN4-KO to EC18, significant differences in FC were found for both RS_{pre} and RS_{post}. In general, HCN4-KO showed significantly increased FC in both RS_{pre} and RS_{post} throughout the whole brain. In RS_{pre}, the most pronounced differences were located in the thalamus, limbic system, amygdala, and hypothalamus. In RS_{post}, these differences extended beyond the above-mentioned regions to cortical areas as well as sensory input, hippocampus, brainstem, and cerebellum.

Intermediate thermal stimulation modulated brain function in RS — increased FC for HCN4-KO and Ctr, decreased FC for EC18

Given that non-salient stimuli can modulate information processing (Kreitz et al. 2018a), we further examined the effect of the intermediate thermal stimulation on the resting-state within each experimental group by comparing RS_{pre} with RS_{post}. NBS revealed significant differences in all three groups (Fig. 7). Ctr showed a widespread, brain-wide increase in FC for RS_{post} (after heat stimulation) relative to RS_{pre} (Fig. 7 **top left**), in particular in olfactory regions, brainstem, sensory input, sensory, and associative cortex, thalamus, hippocampus, amygdala, and hypothalamus. Of note, the left hemisphere showed more modulation, particularly in cortical areas.

Like Ctr, HCN4-KO similarly demonstrated increased FC in RS_{post} compared to RS_{pre} (Fig. 7 **middle left)**, although the effects were more spatially restricted to frontal brain regions: a strong increase in FC was observed in sensory, associative, and motor cortex, as well as in the basal ganglia. Additional increases in FC were observed in some regions of the limbic system, hippocampus, amygdala, and hypothalamus.

In contrast to Ctr and HCN4-KO, EC18 showed a relatively global decrease in FC (Fig. 7 **bottom right)**. Reductions were most prominent in regions of the brainstem, the sensory and associative cortex, as well as in thalamic regions and in the cerebellum.

Discussion

We investigated the role of HCN4 channels to central pain processing using fMRI, comparing a brain-specific HCN4-knockout with acute pharmacological inhibition of the channel. To assess the role of the HCN4 channel in basal brain activity, resting-state fMRI measurements were acquired prior to heat stimulation (RS_{pre}). Compared to Ctr, HCN4-KO exhibited only subtle deviations in intrinsic connectivity relative to Ctr, suggesting that genetic deletion of HCN4 exerts a negligible influence on overall brain function and results in an inherently stable system. After this baseline characterization, we applied staggered heat stimuli to the HCN4-KO and mice subjected to acute HCN4 blockade, enabling a comparison of how chronic versus acute loss of HCN4 function modulates central nociceptive pain processing.

The pain system is broadly organized into ascending and descending pain pathways. The ascending pathway comprises two closely interconnected subsystems, the lateral pain system, which mediates the sensory-discriminative aspects of pain (e.g. localization and intensity), and the medial pain system, which is primarily involved in the affective and evaluative dimensions of pain. Although functionally distinct, these systems operate in a highly coordinated manner (Cross 1994). At lower,

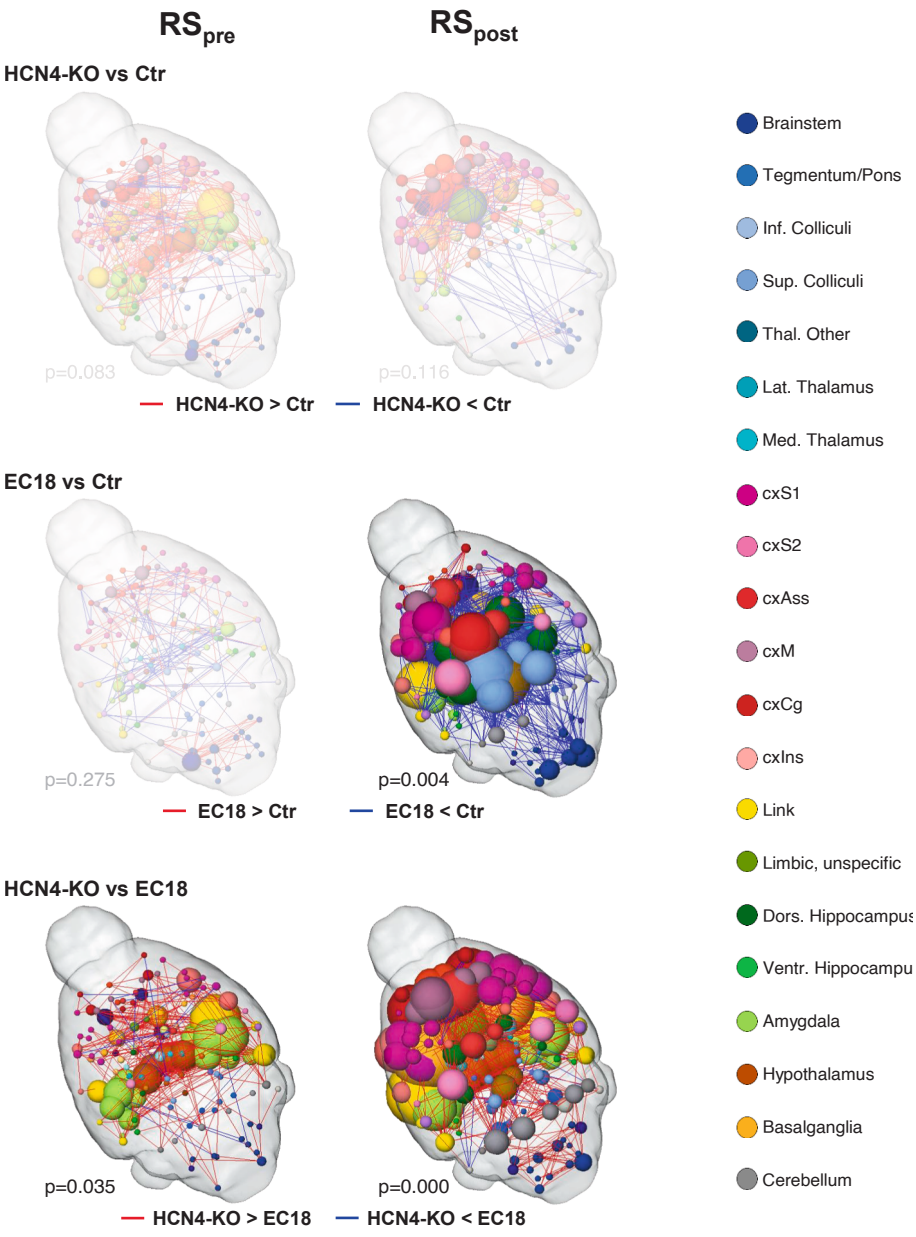

Fig. 6. Differences in functional connectivity for RS-fMRI measurement The differences were calculated using network-based statistics, (p-values as indicated) and displayed as 3D-networks within a transparent brain surface. The 206 brain regions are visualized by the color-coded nodes (orphaned nodes are not shown). The edges between the individual nodes represent the detected differences in functional connectivity (meaning of the color-coded nodes and edges can be seen in the figure). HCN4-KO and Ctr showed no significant differences in FC either in RS_{pre} nor in RS_{post}. Ctr and EC18 also showed no significant differences in RS_{pre} but in RS_{post}. EC18 showed a significantly lower FC across almost all brain regions compared to Ctr. Compared to EC18, HCN4-KO had overall significantly higher FC in RS_{pre} and RS_{post}. In RS_{pre} especially in thalamus, limbic system, amygdala and hypothalamus. In RS_{post}, additionally in sensory and association cortex. Abbreviations: primary somatosensory cortex **(cxS1)**, secondary somatosensory cortex **(cxS2)**, association cortex **(cxAss)**, motor cortex **(cxM)**, cingulate cortex **(cxCg)**, insular cortex **(cxIns)**.

innocuous temperatures (40 °C and 45 °C), pain processing is dominated by the lateral pathway, which governs stimulus localization. At higher, noxious temperatures (50 °C and 54 °C), the medial pain system becomes increasingly engaged, reflecting the enhanced emotional-affective component of pain perception (Sergejeva and Hess 2008). By employing a staggered temperature paradigm, our study allowed a characterization of the distinct response properties of the medial and lateral pain systems in the event of HCN4 loss.

Incoming stimuli from the peripheral nociceptors are relayed through the lateral spinothalamocortical pathway, which transmits signals from the lateral thalamus (Groh et al. 2018) to the somatosensory cortex, among others (Bourne, Machado, and Nagel 2014; Kulkarni et al. 2005; Groh et al. 2018). Within this circuitry, the somatosensory cortex is responsible for the precise localization of the stimulus and for evaluating its intensity. In our study, the significant increase in IWV at 45 °C together with significant alterations in node-specific parameters and functional connectivity within these sensory-processing regions strongly suggests that the KO modulates early, sensory-discriminative components of pain perception.

The descending pain pathway serves as a critical feedback system, with its associated brain regions exerting substantial influence over pain perception (Zhuo and Gebhart 1997). In addition to differences observed in the sensory cortex, our data revealed significant IWV alterations at 45 °C in structures of the sensory input and the cerebellum. Both regions

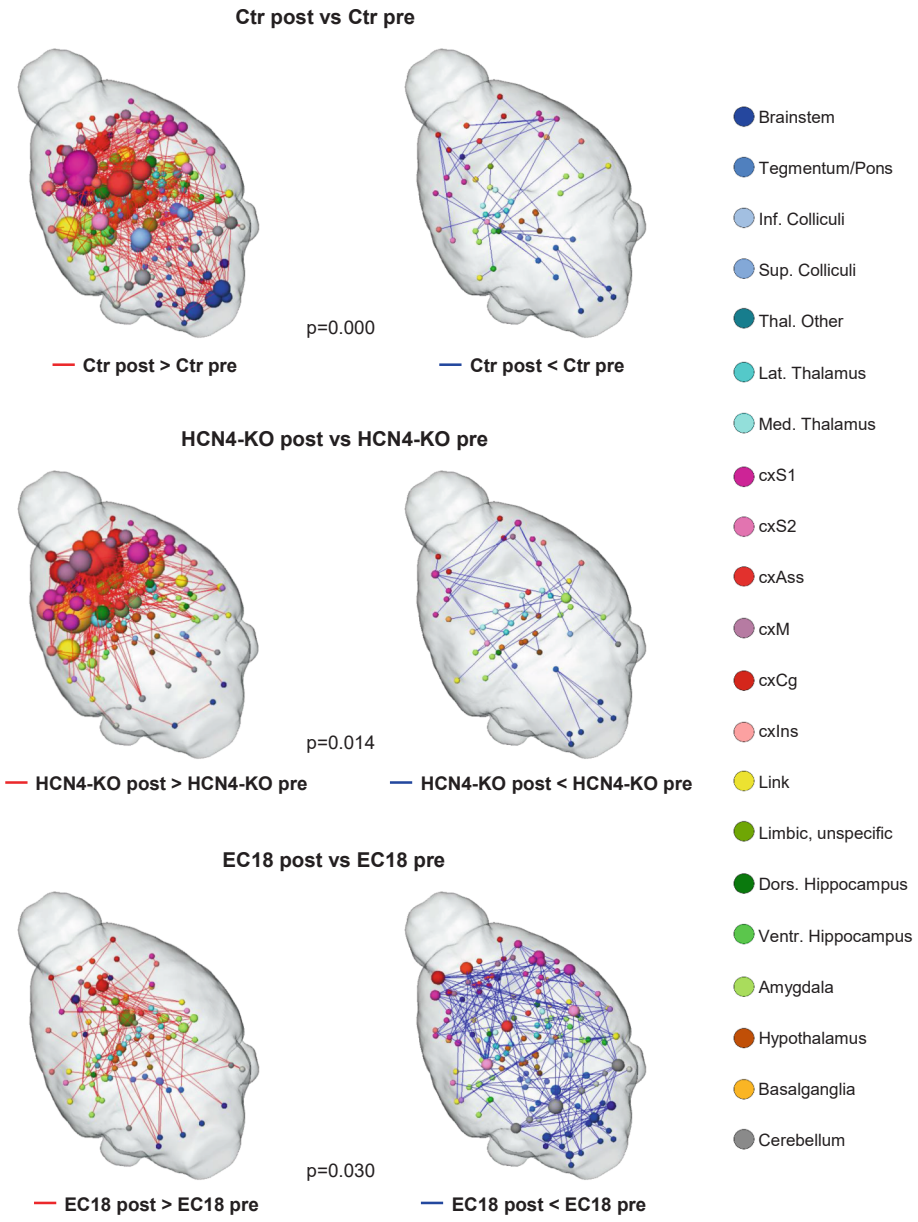

Fig. 7. Influence of the interposed stimulation on the resting-state – Comparison of RS_{pre} and RS_{pos}. Comparison of RS_{pre} and RS_{post} was carried out within the same group. The differences were calculated using network-based statistics, (p-values as indicated) and displayed as 3D-networks within a transparent brain surface. The 206 brain regions are visualized by the color-coded nodes (orphaned nodes are not shown). The edges between the individual nodes represent the differences in functional connectivity (meaning of the color-coded nodes and edges can be seen in the figure). Significant differences in FC between RS_{post} and RS_{pre} can be observed for all groups. While Ctr and HCN4-KO showed a significant increase in FC in a large part of the brain regions, EC18 showed the opposite – seen over the whole brain, there was predominantly a decrease in FC. Abbreviations: primary somatosensory cortex **(cxS1)**, secondary somatosensory cortex **(cxS2)**, association cortex **(cxAss)**, motor cortex **(cxM)**, cingulate cortex **(cxCg)**, insular cortex **(cxIns)**.

maintain functional connections to the descending pain pathway, directly in the case of the cerebellum, and indirectly through sensory input regions such as the ventral tegmental area (VTA) (Flores-García et al. 2023; Li et al. 2024). The VTA, as a central component of the mesolimbic dopamine circuit, interacts closely with the hypothalamus and functions as a key integrative hub (Flores-García et al. 2023). The mesolimbic dopamine circuit plays a pivotal role in modulating both emotional states and pain processing (Ma et al. 2023), with painful stimuli generally eliciting increased VTA activation (Wanigasekera et al. 2012).

Endogenous pain inhibition, an essential component of the descending pain system, is typically not triggered at temperatures below 45 °C (You et al. 2014). Thus, the increased IWV and significant differences in the node-specific parameters in HCN4-KO within areas of the sensory input and cerebellum at 45 °C indicate an enhanced perception of pain, even to weak thermal stimuli.

At 50 °C, processing shifts from regions primarily responsible for stimulus perception towards those mediating the affective and regulatory aspects of pain. Specifically, regions of the descending pain system, including the limbic system (amygdala and hypothalamus) and the prefrontal cortex (associative cortex), interconnected via the PAG, become more important (Groh et al. 2018; Kulkarni et al. 2005; Freund et al. 2009). In these areas, the EC18 group displayed significantly lower IWV and reduced node-specific parameters compared to HCN4-KO and Ctr. This may reflect a diminished perception of noxious heat (50 °C), where reduced pain experience leads to less engagement of emotional and inhibitory descending processes. The convergence of values between HCN4-KO and Ctr at 50 °C further indicates that the thermal

hypersensitivity of HCN4-KO is confined to lower temperatures, whereas responses to noxious stimuli resemble those of Ctr.

Since even transient sensory stimuli can leave lasting impressions on brain circuitry and contribute to memory encoding, resting-state measurements were conducted following the s-fMRI (Kreitz et al. 2018b; Wank et al. 2022; Kreitz et al. 2022). HCN4-KO did not show any significant differences in global RS network properties and functional connectivity compared to Ctr, suggesting that the impact of the KO is largely limited to modulating brain function during the thermal stimulation itself.

In contrast, in a comparison of RS_{pre} and RS_{post} the EC18 group showed altered general network characteristics. FC was significantly lower in regions associated with pain processing and suppression (PAG, associative cortex, sensory cortex, amygdala) accompanied by significant differences in node-specific parameters. These findings indicate a strong acute modulatory effect of EC18 on post-stimulus network dynamics, potentially affecting memory encoding following noxious events.

Within-group RS_{post} v.s. RS_{pre} comparisons further support this interpretation: both HCN4-KO and Ctr exhibited widespread increase in FC after stimulation, whereas EC18 showed the opposite, consistent with limited or absent memory encoding in relation to painful events (Fig. 7).

In a previous study examining the role of HCN4 in epilepsy, a reduction of HCN4 expression and pharmacological inhibition by EC18 led to a decreased seizure susceptibility (Kharouf et al. 2020). This contrasts our experiments where pharmacological blockade of the HCN4 channel by EC18 led to a reduction in nociception (thermal hyposensitive phenotype), whereas knockout of HCN4 led to a thermal hypersensitive phenotype. It should be noted that different mouse lines were used. Kharouf et al. employed a tamoxifen-inducible line resulting in a significant reduction of HCN4, however the channel protein was still present in cortex and thalamus (~15–20 %). We used a line with a complete deletion of HCN4 in all brain regions (Zobeiri et al., 2019).

Regarding the pharmacokinetic profile of EC18, Kharouf et al. reported that following i.p. administration, concentrations decline with a marked reduction in plasma within 60 min and in the brain within 30 min. However, their study also demonstrated that the substantially diminished brain concentrations 30 min post-injection were still sufficient to elicit significant anticonvulsant effects in different seizure models. This indicates that EC18 remains functionally active in vivo even at theoretically sub-saturating central concentrations. This is also consistent with our results, which show that the BOLD signal in the EC18 group remains stable throughout the entire 50 min measurement period. No return to baseline or other shifts were observed at later times during the scan. This confirms that the modulatory effect of EC18 was active throughout the entire protocol (**Fig. S2**). In line with this hypothesis, in vitro recordings showed no recovery of the current after a 10 min washout of EC18 (Del Lungo et al. 2012) indicating a long-lasting blocking effect of the drug which is not quickly reversed when the concentration decreases. Furthermore, if the issue were merely insufficient target engagement, one would expect a blunted phenotype similar to the genetic knockout. The fact that we observe qualitatively divergent outcomes suggests that reduced brain concentrations are unlikely to explain the difference between EC18 treatment and HCN4 knockout in pain processing.

A possible explanation for the divergent results between the HCN4-KO and pharmacological inhibition by EC18 could be related to the limited selectivity of the substance. Although EC18 is currently the best available and most extensively validated HCN4-preferring blocker, its isoform selectivity is modest.

In HCN-isoform expressing HEK 293 cells, EC18 inhibited HCN4 with an EC_{50} of 3.9 μM, while the corresponding values for HCN1 and HCN2 are 21.0 μM and 19.4 μM, respectively (Del Lungo et al. 2012; Romanelli et al. 2019). These data indicate a selectivity ratio of about fivefold.

Consequently, EC18 may also exert some mild inhibitory effects on HCN1 and HCN2. We cannot rule out that a partial co-inhibition contributes to the discrepancies between genetic deletion and pharmacological blockade. Nevertheless, the robust central hypoalgesic effects of EC18 underscore that an HCN4-targeted modulation is a promising strategy in the development of centrally acting analgesic drugs.

Another critical factor contributing to the thermal-hypersensitive phenotype of HCN4-KO mice is the developmental role of the channel. HCN4 expression is known to be elevated during early postnatal stages before declining with age (Brewster et al. 2007; Kanyshkova et al. 2009). Consequently, constitutive deletion of the channel may engage compensatory processes that fundamentally alter the maturation of neuronal networks (Butz, Worgotter, and van Ooyen 2009; Trachtenberg et al. 2002).

Neurobiologically, the absence of HCN4-mediated pacemaking or oscillatory activity during these critical windows could trigger maladaptive homeostatic plasticity. This might involve compensatory upregulation of other subunits (e.g., HCN1/2) or structural remodeling of synaptic connectivity to offset the loss of intrinsic excitability. Notably, HCN4 deficits have been linked to hyperexcitable states, such as infantile forms of epilepsy (Campostrini et al. 2018). It is therefore plausible that similar pro-excitatory network reorganizations may occur in the somatosensory system of the KO mice, leading to the observed central sensitization and pain hypersensitivity. This stands in sharp contrast to the acute effects of EC18, which inhibits the channel in a mature, normally organized brain network, resulting in hypoalgesia.

A general potential confounding factor in fMRI experiments is the influence of anesthesia on brain function. To mitigate such effects, we chose low-dose isoflurane anesthesia, which provides the best compromise between minimizing interference with cerebral blood flow and neurotransmitter signaling, while maintaining a controllable, easily adaptable and only minimally analgesic anesthetic state (Lenz et al. 1998; Masamoto et al. 2009). Compared with other anesthetics, the effect of isoflurane on general brain activity is generally small, making it particularly suitable for studies of resting-state and stimulus-evoked fMRI. To ensure experimental consistency and comparability of the results, all animals were maintained under the same anesthetic regime during the fMRI experiments. No major adjustment of the isoflurane dose between animals was necessary to ensure a stable respiration rate. Importantly, although animal fMRI experiments are usually performed under anesthesia, while human fMRI is usually performed in the awake state, previous studies have demonstrated that the results of fMRI experiments in mice are generally well translatable to humans (Hess et al. 2011; Sierakowiak et al. 2015).

Taken together, our findings demonstrate that HCN4 channels are highly involved in modulating central pain processing, as both genetic deletion and pharmacological inhibition significantly alter the perception and processing of noxious thermal stimuli. The knockout leads to thermal hypersensitivity, reflected in increased BOLD IWV and graph-theoretical parameters during stimulation, while resting-state activity remains stable.

In contrast, pharmacological blockade with EC18 reduces nociception, evident in lower IWV, and primarily affects resting-state connectivity rather than stimulus-driven responses. These divergent effects may either result from long-term compensatory adaptations in the knockout which are absent in the acutely treated EC18 animals, or from limited channel selectivity of EC18. Overall, our findings underscore a critical distinction between genetic models and a pharmacological intervention.

Fundings

This research did not receive any specific grant from funding agencies in the public, commercial, or not-for-profit sectors.

Data availability

The data that support the findings of this study are available from the

corresponding author upon reasonable request.

CRediT authorship contribution statement

Maximilian Häfele: Writing – review & editing, Writing – original draft, Methodology, Investigation, Formal analysis, Conceptualization. **Natalia K. Freus:** Writing – review & editing, Writing – original draft. **Silke Kreitz:** Writing – review & editing, Formal analysis. **Maria Novella Romanelli:** Writing – review & editing, Resources. **Andreas Ludwig:** Writing – review & editing, Conceptualization. **Isabel Wank:** Writing – review & editing, Conceptualization. **Andreas Hess:** Writing – review & editing, Conceptualization.

Acknowledgements

We would like to thank Beate Layh for rearing and providing the experimental animals.

Appendix A. Supplementary data

Supplementary data to this article can be found online at https://doi.org/10.1016/j.neuroscience.2026.01.011.

References

Bourne, S., Machado, A.G., Nagel, S.J., 2014. Basic anatomy and physiology of pain pathways. Neurosurg. Clin. N. Am. 25, 629–638.
Brewster, A.L., Chen, Y., Bender, R.A., Yeh, A., Shigemoto, R., Baram, T.Z., 2007. Quantitative analysis and subcellular distribution of mRNA and protein expression of the hyperpolarization-activated cyclic nucleotide-gated channels throughout development in rat hippocampus. Cereb. Cortex 17, 702–712.
Butz, M., Worgotter, F., van Ooyen, A., 2009. Activity-dependent structural plasticity. Brain Res. Rev. 60, 287–305.
Campostrini, G., DiFrancesco, J.C., Castellotti, B., Milanesi, R., Gnecchi-Ruscone, T., Bonzanni, M., Bucchi, A., Baruscotti, M., Ferrarese, C., Franceschetti, S., Canafoglia, L., Ragona, F., Freri, E., Labate, A., Gambardella, A., Costa, C., Gellera, C., Granata, T., Barbuti, A., DiFrancesco, D., 2018. A Loss-of-function HCN4 mutation associated with familial benign myoclonic epilepsy in infancy causes increased neuronal excitability. Front. Mol. Neurosci. 11, 269.
Cross, Shelley A., 1994. Pathophysiology of pain.“ In Mayo Clinic Proceedings, 375-83. Elsevier.
Del Lungo, M., Melchiorre, M., Guandalini, L., Sartiani, L., Mugelli, A., Koncz, I., Szel, T., Varro, A., Romanelli, M.N., Cerbai, E., 2012. Novel blockers of hyperpolarization-activated current with isoform selectivity in recombinant cells and native tissue. Br. J. Pharmacol. 166, 602–616.
Emery, E.C., Young, G.T., Berrocoso, E.M., Chen, L., McNaughton, P.A., 2011. HCN2 ion channels play a central role in inflammatory and neuropathic pain. Science 333, 1462–1466.
Estrada, Ernesto, 2006. Network robustness to targeted attacks. The interplay of expansibility and degree distribution. The European Physical Journal B-Condensed Matter and Complex Systems, 52: 563-74.
Flores-García, M., Rizzo, A., Garçon-Poca, M.Z., Fernández-Dueñas, V., Bonaventura, J., 2023. Converging circuits between pain and depression: the ventral tegmental area as a therapeutic hub. Front. Pharmacol. 14, 1278023.
Fox, M.D., Zhang, D., Snyder, A.Z., Raichle, M.E., 2009. The global signal and observed anticorrelated resting state brain networks. J. Neurophysiol. 101, 3270–3283.
Franklin, K.B.J., Paxinos, G., 2008. The mouse brain in stereotaxic coordinates, Third edit. ed. Menzel J.“ In.: Academic Press, Elsevier, New York, NY.
Freitas, S., Yang, D., Kumar, S., Tong, H., Chau, D.H., 2022. Graph vulnerability and robustness: a survey. IEEE Trans. Knowl. Data Eng. 35, 5915–5934.
Freund, W., Klug, R., Weber, F., Stuber, G., Schmitz, B., Wunderlich, A.P., 2009. Perception and suppression of thermally induced pain: a fMRI study. Somatosens. Mot. Res. 26, 1–10.
Groh, A., Krieger, P., Mease, R.A., Henderson, L., 2018. Acute and chronic pain processing in the thalamocortical system of humans and animal models. Neuroscience 387, 58–71.
Häfele, M., Kreitz, S., Ludwig, A., Hess, A., Wank, I., 2023. The impact of HCN4 channels on CNS brain networks as a new target in pain development. Front. Netw. Physiol. 3, 1090502.
Hammelrath, L., Skokic, S., Khmelinskii, A., Hess, A., van der Knaap, N., Staring, M., Lelieveldt, B.P.F., Wiedermann, D., Hoehn, M., 2016. Morphological maturation of the mouse brain: an in vivo MRI and histology investigation. Neuroimage 125, 144–152.
Heintz, N., 2004. Gene expression nervous system atlas (GENSAT). Nat. Neurosci. 7, 483.
Herrmann, S., Rajab, H., Christ, I., Schirdewahn, C., Hofler, D., Fischer, M.J.M., Bruno, A., Fenske, S., Gruner, C., Kramer, F., Wachsmann, T., Wahl-Schott, C., Stieber, J., Biel, M., Ludwig, A., 2017. Protein kinase a regulates inflammatory pain sensitization by modulating HCN2 channel activity in nociceptive sensory neurons. Pain 158, 2012–2024.
Herrmann, S., Stieber, J., Ludwig, A., 2007. Pathophysiology of HCN channels. Pflugers Arch. 454, 517–522.
Hess, A., Axmann, R., Rech, J., Finzel, S., Heindl, C., Kreitz, S., Sergeeva, M., Saake, M., Garcia, M., Kollias, G., Straub, R.H., Sporns, O., Doerfler, A., Brune, K., Schett, G., 2011. Blockade of TNF-alpha rapidly inhibits pain responses in the central nervous system. PNAS 108, 3731–3736.
Hughes, D.I., Boyle, K.A., Kinnon, C.M., Bilsland, C., Quayle, J.A., Callister, R.J., Graham, B.A., 2013. HCN4 subunit expression in fast-spiking interneurons of the rat spinal cord and hippocampus. Neuroscience 237, 7–18.
Jun, W.U., Barahona, M., Yue-Jin, T., Hong-Zhong, D., 2010. Natural connectivity of complex networks. Chin. Phys. Lett. 27, 078902.
Kanyshkova, T., Pawlowski, M., Meuth, P., Dube, C., Bender, R.A., Brewster, A.L., Baumann, A., Baram, T.Z., Pape, H.C., Budde, T., 2009. Postnatal expression pattern of HCN channel isoforms in thalamic neurons: relationship to maturation of thalamocortical oscillations. J. Neurosci. 29, 8847–8857.
Kharouf, Q., Phillips, A.M., Bleakley, L.E., Morrisroe, E., Oyrer, J., Jia, L.H., Ludwig, A., Jin, L., Nicolazzo, J.A., Cerbai, E., Romanelli, M.N., Petrou, S., Reid, C.A., 2020. The hyperpolarization-activated cyclic nucleotide-gated 4 channel as a potential anti-seizure drug target. Br. J. Pharmacol. 177, 3712–3729.
Kreitz, S., de Celis Alonso, B., Uder, M., Hess, A., 2018a. A New analysis of resting state connectivity and graph theory reveals distinctive short-term modulations due to whisker stimulation in rats. Front. Neurosci. 12, 334.
Kreitz, S., de Celis, B., Alonso, M.U., Hess, A., 2018b. A new analysis of resting state connectivity and graph theory reveals distinctive short-term modulations due to whisker stimulation in rats. Front. Neurosci. 12, 334.
Kreitz, Silke, Angelika Mennecke, Laura Konerth, Julie Rösch, Armin M Nagel, Frederik B Laun, Michael Uder, Arnd Dörfler, and Andreas Hess. 2022. 'Capturing early human memory consolidation utilizing the higher functional specificity of 7T compared to 3T-fMRI', *bioRxiv*: 2022.02. 01.478615.
Kulkarni, B., Bentley, D.E., Elliott, R., Youell, P., Watson, A., Derbyshire, S.W., Frackowiak, R.S., Friston, K.J., Jones, A.K., 2005. Attention to pain localization and unpleasantness discriminates the functions of the medial and lateral pain systems. Eur. J. Neurosci. 21, 3133–3142.
Leicht, E.A., Holme, P., Newman, M.E., 2006. Vertex similarity in networks. Phys. Rev. E Stat. Nonlin. Soft Matter Phys. 73, 026120.
Lenz, C., Rebel, A., van Ackern, K., Kuschinsky, W., Waschke, K.F., 1998. Local cerebral blood flow, local cerebral glucose utilization, and flow-metabolism coupling during sevoflurane versus isoflurane anesthesia in rats. Anesthesiology 89, 1480–1488.
Li, C.N., Keay, K.A., Henderson, L.A., Mychasiuk, R., 2024. Re-examining the mysterious role of the cerebellum in pain. J. Neurosci. 44.
Ludwig, A., Zong, X., Stieber, J., Hullin, R., Hofmann, F., Biel, M., 1999. Two pacemaker channels from human heart with profoundly different activation kinetics. EMBO J. 18, 2323–2329.
Ma, Y., Zhao, W., Chen, D., Zhou, D., Gao, Y., Bian, Y., Xu, Y., Xia, S.H., Fang, T., Yang, J. X., Song, L., Liu, H., Ding, H.L., Zhang, H., Cao, J.L., 2023. Disinhibition of Mesolimbic Dopamine Circuit by the Lateral Hypothalamus Regulates Pain Sensation. J. Neurosci. 43, 4525–4540.
Masamoto, K., Fukuda, M., Vazquez, A., Kim, S.G., 2009. Dose-dependent effect of isoflurane on neurovascular coupling in rat cerebral cortex. Eur. J. Neurosci. 30, 242–250.
Monteggia, L.M., Eisch, A.J., Tang, M.D., Kaczmarek, L.K., Nestler, E.J., 2000. Cloning and localization of the hyperpolarization-activated cyclic nucleotide-gated channel family in rat brain. Brain Res. Mol. Brain Res. 81, 129–139.
Moosmang, S., Biel, M., Hofmann, F., Ludwig, A., 1999. Differential distribution of four hyperpolarization-activated cation channels in mouse brain. Biol. Chem. 380, 975–980.
Newman, M.E., 2002. Assortative mixing in networks. Phys. Rev. Lett. 89, 208701.
Patberg, M., Oniani, T., Disse, P., Peischard, S., Vinnenberg, L., Zobeiri, M., Romanelli, M.N., Epping, L., Wiendl, H., Meuth, S.G., Hundehege, P., Seebohm, G., Budde, T., Junker, A., 2023. Optimized synthesis and pharmacological evaluation of HCN channel inhibitor EC18. Arch Pharm (weinheim) 356, e2200665.
Romanelli, Maria Novella, Martina Del Lungo, Luca Guandalini, Mehrnoush Zobeiri, András Gyökeres, Tamás Árpádffy-Lovas, Istvan Koncz, Laura Sartiani, Gianluca Bartolucci, and Silvia Dei. 2019. 'EC18 as a tool to understand the role of HCN4 channels in mediating hyperpolarization-activated current in tissues, ACS Med. Chem. Lett. 10: 584-89.
Santoro, B., Chen, S., Luthi, A., Pavlidis, P., Shumyatsky, G.P., Tibbs, G.R., Siegelbaum, S. A., 2000. Molecular and functional heterogeneity of hyperpolarization-activated pacemaker channels in the mouse CNS. J. Neurosci. 20, 5264–5275.
Santos-Vera, B., Vaquer-Alicea, A.D.C., Maria-Rios, C.E., Montiel-Ramos, A., Ramos-Cardona, A., Vazquez-Torres, R., Sanabria, P., Jimenez-Rivera, C.A., 2019. Protein and surface expression of HCN2 and HCN4 subunits in mesocorticolimbic areas after cocaine sensitization. Neurochem. Int. 125, 91–98.
Schnorr, Sabine, Mirjam Eberhardt, Katrin Kistner, Hamsa Rajab, Johannes Käßer, Andreas Hess, Peter Reeh, Andreas Ludwig, and Stefan Herrmann. 2014. 'HCN2 channels account for mechanical (but not heat) hyperalgesia during long-standing inflammation', *PAIN*®, 155: 1079-90.
Sergejeva, M., Hess, A., 2008. Cerebral representation of hyperalgesia: evidence from functional imaging in humans and animals. Neurosci. Imaging Res. Trends 7.
Sherman, S.M., Guillery, R.W., 2002. The role of the thalamus in the flow of information to the cortex. Philos. Trans. R. Soc. Lond. B Biol. Sci. 357, 1695–1708.
Sierakowiak, A., Monnot, C., Aski, S.N., Uppman, M., Li, T.Q., Damberg, P., Brene, S., 2015. Default mode network, motor network, dorsal and ventral basal ganglia

networks in the rat brain: comparison to human networks using resting state-fMRI. PLoS One 10, e0120345.
Stieber, Juliane, Stefan Herrmann, Susanne Feil, Jana Löster, Robert Feil, Martin Biel, Franz Hofmann, Andreas Ludwig, 2003. The hyperpolarization-activated channel HCN4 is required for the generation of pacemaker action potentials in the embryonic heart. Proc. Natl. Acad. Sci. 100: 15235-40.
Trachtenberg, J.T., Chen, B.E., Knott, G.W., Feng, G., Sanes, J.R., Welker, E., Svoboda, K., 2002. Long-term in vivo imaging of experience-dependent synaptic plasticity in adult cortex. Nature 420, 788–794.
Tronche, F., Kellendonk, C., Kretz, O., Gass, P., Anlag, K., Orban, P.C., Bock, R., Klein, R., Schutz, G., 1999. Disruption of the glucocorticoid receptor gene in the nervous system results in reduced anxiety. Nat. Genet. 23, 99–103.
Tsantoulas, C., Mooney, E.R., McNaughton, P.A., 2016. HCN2 ion channels: basic science opens up possibilities for therapeutic intervention in neuropathic pain. Biochem. J 473, 2717–2736.
Wang, S., Zhang, J., Yue, X., 2018. Multiple robustness assessment method for understanding structural and functional characteristics of the power network. Physica A 510, 261–270.
Wanigasekera, V., Lee, M.C., Rogers, R., Kong, Y., Leknes, S., Andersson, J., Tracey, I., 2012. Baseline reward circuitry activity and trait reward responsiveness predict expression of opioid analgesia in healthy subjects. PNAS 109, 17705–17710.
Wank, I., Kutsche, L., Kreitz, S., Reeh, P., Hess, A., 2022. Imaging the influence of peripheral TRPV1-signaling on cerebral nociceptive processing applying fMRI-based graph theory in a resiniferatoxin rat model. PLoS One 17, e0266669.
Watts, D.J., Strogatz, S.H., 1998. Collective dynamics of 'small-world' networks. Nature 393, 440–442.
You, H.J., Lei, J., Ye, G., Fan, X.L., Li, Q., 2014. Influence of intramuscular heat stimulation on modulation of nociception: complex role of central opioid receptors in descending facilitation and inhibition. J. Physiol. 592, 4365–4380.
Zalesky, A., Fornito, A., Bullmore, E.T., 2010. Network-based statistic: identifying differences in brain networks. Neuroimage 53, 1197–1207.
Zhuo, M., Gebhart, G.F., 1997. Biphasic modulation of spinal nociceptive transmission from the medullary raphe nuclei in the rat. J. Neurophysiol. 78, 746–758.
Zobeiri, M., Chaudhary, R., Blaich, A., Rottmann, M., Herrmann, S., Meuth, P., Bista, P., Kanyshkova, T., Lüttjohann, A., Narayanan, V., 2019. The hyperpolarization-activated HCN4 channel is important for proper maintenance of oscillatory activity in the thalamocortical system. Cereb. Cortex 29, 2291–2304.
Zuniga, R., Gonzalez, D., Valenzuela, C., Brown, N., Zuniga, L., 2016. Expression and cellular localization of HCN channels in rat cerebellar granule neurons. Biochem. Biophys. Res. Commun. 478, 1429–1435.